Ko et al. *NPG Asia Materials* _####################_
DOI 10.1038/s41427-018-0020-y

NPG Asia Materials

ARTICLE Open Access

# Understanding the structural, electrical, and optical properties of monolayer *h*-phase $RuO_2$ nanosheets: a combined experimental and computational study

Dong-Su Ko[1], Woo-Jin Lee[1], Soohwan Sul[1], Changhoon Jung[1], Dong-Jin Yun[1], Hee-Goo Kim[1], Won-Joon Son[1], Jae Gwan Chung[1], Doh Won Jung[2], Se Yun Kim[2], Jeongmin Kim[3], Wooyoung Lee[3], Chan Kwak[2], Jai Kwang Shin[1], Jung-Hwa Kim[1] and Jong Wook Roh[4]

## Abstract

The structural, electrical, and optical properties of monolayer ruthenium oxide ($RuO_2$) nanosheets (NSs) fabricated by chemical exfoliation of a layered three-dimensional form of K-intercalated $RuO_2$ are studied systematically via experimental and computational methods. Monolayer $RuO_2$ NS is identified as having a distorted *h*-$MX_2$ structure. This is the first observation of a $RuO_2$ NS structure that is unlike the *t*-$MX_2$ structure of the $RuO_2$ layers in the parent material and does not have hexagonal symmetry. The distorted *h*-$MX_2$ $RuO_2$ NSs are shown to have optical transparency superior to that of graphene, thereby predicting the feasibility of applying $RuO_2$ NSs to flexible transparent electrodes. In addition, it is demonstrated that the semiconducting band structures of $RuO_2$ NSs can be manipulated to be semi-metallic by adjusting the crystal structure, which is related to band-gap engineering. This finding indicates that $RuO_2$ NSs can be used in a variety of applications, such as flexible transparent electrodes, atomic-layer devices, and optoelectronic devices.

## Introduction

Since the discovery of graphene, two-dimensional (2D) materials, including hexagonal boron nitride and transition metal dichalcogenides and 2D metal oxides, have attracted enormous attention for their potential in electronic, mechanical, and optoelectronic applications because of their unique and outstanding properties[1–5]. In particular, nanostructured metal oxide materials, including 2D nanosheets (NSs), have shown significant importance in a wide range of applications, such as catalysis[6], solar cells[7], supercapacitors[8], and energy storage devices[9–12]. Exfoliation techniques have opened up opportunities for fabricating new 2D metal oxide NSs by manufacturing monolayer NSs from three-dimensional (3D)-layered parent materials.

Bulk ruthenium oxide ($RuO_2$) has a well-known 3D rutile crystal structure with metallic behavior that has drawn considerable attention not only in academic research, but also in industry due to its thermodynamic stability, semi-transparency, and distinctive metallic properties[13,14]. In recent years, $RuO_2$ NSs exfoliated from bulk rutile $RuO_2$ have been used in lithium–oxygen and lithium–ion battery applications because exfoliation facilitates the fabrication of NSs[15,16]. Wang et al.[17] reported obtaining a sheet resistance of 4.1 kΩ $sq^{-1}$ from $RuO_2$ NS films at room temperature, although most of their work focused on all NS ultrathin capacitors. Recently, Lee et al.[18] also demonstrated the optimization

Correspondence: Jung-Hwa Kim (jh1179.kim@samsung.com) or Jong Wook Roh (jw.roh@knu.ac.kr)
[1]Platform Technology Lab, Samsung Advanced Institute of Technology, 130 Samsung-ro, Yeongtong-gu, Suwon-si, Gyeonggi-do 16678, Republic of Korea
[2]Inorganic Materials Lab, Samsung Advanced Institute of Technology, 130 Samsung-ro, Yeongtong-gu, Suwon-si, Gyeonggi-do 16678, Republic of Korea
Full list of author information is available at the end of the article

© The Author(s) 2018
**Open Access** This article is licensed under a Creative Commons Attribution 4.0 International License, which permits use, sharing, adaptation, distribution and reproduction in any medium or format, as long as you give appropriate credit to the original author(s) and the source, provide a link to the Creative Commons license, and indicate if changes were made. The images or other third party material in this article are included in the article's Creative Commons license, unless indicated otherwise in a credit line to the material. If material is not included in the article's Creative Commons license and your intended use is not permitted by statutory regulation or exceeds the permitted use, you will need to obtain permission directly from the copyright holder. To view a copy of this license, visit http://creativecommons.org/licenses/by/4.0/.

of electrode performance using exfoliated 2D $RuO_2$ NSs as a conducting additive. Choi et al.[19] investigated the detection of $NO_2$ gas using films of $RuO_2$ NSs, which showed potential as a chemical sensor. However, these researchers only focused on the properties of $RuO_2$ NS assemblies rather than on the properties of an individual monolayer $RuO_2$ NS because of the difficulty of investigating an individual monolayer NS. In fact, although the characterization of the structural, electrical, and optical properties of monolayer discrete $RuO_2$ NSs is critical to the prediction of feasibility of applying $RuO_2$ NSs to atomic-layer devices, thus far, their detailed crystal structures and physical properties have remained largely unknown. It should be noted that NSs exfoliated from parent materials could have crystal structures different from that of their parent material, resulting in physical properties that differ from those of the bulk material. Because determining the crystal structure of an NS is not trivial, it has only been suggested that $RuO_2$ NSs have crystal structures that differ from that of rutile $RuO_2$, which is thought to be hexagonal[20].

Here, we report the first systematic study of the crystal structure and physical properties of individual monolayer $RuO_2$ NSs through experimental and computational methods. A combination of transmission electron microscopy (TEM), X-ray diffraction (XRD), and first-principles calculation techniques shows that individual monolayer $RuO_2$ NSs have distorted *h*-$MX_2$ structures (trigonal prismatic coordination between the M and X atoms), whereas the parent $K_{0.25}RuO_2$ contains $RuO_2$ layers with *t*-$MX_2$ structures (octahedral phase coordination). First-principles calculations and experimental results show that the distorted *h*-$MX_2$ monolayer $RuO_2$ NSs are semiconductors with an average transmittance in the visible wavelength range, which is 1% higher than that of monolayer graphene. In addition, we demonstrate that the electrical properties of monolayer $RuO_2$ NSs can be adjusted by manipulating their structural distortion. Thus, our results suggest that distorted *h*-$RuO_2$ NSs have potential in electrical and optical device applications.

## Results and discussion

### Identification of crystal structure of K-intercalated $RuO_2$

The crystal structure of most exfoliated NSs resembles that of the parent layer materials. Therefore, identification of the parent crystal structures is essential. We synthesized a 3D-layered material of K-intercalated $RuO_2$ (designated as K-form $RuO_2$) as the parent material. Since the crystal structure of K-form $RuO_2$ has not been systemically investigated, we identified the crystal structure of K-form $RuO_2$ by carrying out a Rietveld refinement analysis of the XRD and scanning transmission electron microscopy–annular bright-field (STEM–ABF) with X-ray energy-dispersive spectroscopy (XEDS). We found that bulk K-form $RuO_2$ has a monoclinic phase with a K–O–Ru–O–K–O–Ru–O–K layered stacking sequence along the *c*-axis in each unit cell (Figures S1 and S2). Subsequently, we investigated whether the Ru–O atomic configuration in K-form $RuO_2$ is *t*-$MX_2$ or *h*-$MX_2$. Due to the experimental limits (such as the inability of XRD refinements and SADP (selected area diffraction pattern) to distinguish between the *h*- and *t*-phases), accurate determination of oxygen atomic positions along the *c*-axis is difficult. To overcome this obstacle, first-principles calculations have been applied to determine the atomic configuration through optimizing the structure. We found the *t*-$MX_2$-type Ru–O configuration to be stable in $K_{0.25}RuO_2$, whereas the *h*-$MX_2$ configuration is unstable and changes to *t*-$MX_2$ after structural optimization (Figure S3). Thus, $K_{0.25}RuO_2$ should have the *t*-$MX_2$-type Ru–O configuration. The optimal crystal structure of $K_{0.25}RuO_2$ is illustrated in Figure S2b.

### Identification of crystal structure of monolayer $RuO_2$ NSs

K-form $RuO_2$ was used as a parent material for the synthesis of the $RuO_2$ NSs by chemical exfoliation. Additional details on the exfoliating method are provided in the "Methods" section. The electron diffraction patterns observed using TEM revealed that all the $RuO_2$ NSs had identical patterns with nearly the same lattice parameters (i.e., their parameters differed by less than 1%). The $RuO_2$ NSs exfoliated from the K-form $RuO_2$ with a lateral length of several hundred micrometers, as shown in Fig. 1a, and had a lateral width of a few tens of micrometers. This large monolayer size is advantageous for fabricating and manipulating NS-based electronic and photonic devices[21]. Exfoliated $RuO_2$ NSs with a width of several tens of micrometers dispersed on a Quantifoil TEM grid and $SiO_2$-deposited Si wafer were observed by performing STEM–ADF imaging and atomic force microscopy (AFM), and the results are shown in Fig. 1b, c, respectively. The thickness of the monolayer $RuO_2$ NSs was measured by AFM to be approximately 0.65 nm. This result is consistent with the interlayer distance in the re-stacked $RuO_2$ NSs obtained from the STEM–ADF image presented in Fig. 1d. The re-stacked NSs were fabricated on a glass substrate by alternating drop-casting and drying processes. Thus, the AFM and TEM results provide evidence that we were successful in exfoliating uniform monolayer $RuO_2$ NSs.

The monolayer $RuO_2$ NSs were investigated by conducting TEM analysis of flat and uniform areas, as shown in Fig. 1b. The atomic structure of the $RuO_2$ NSs was observed directly by carrying out monochromated Cs-corrected high-resolution TEM (HRTEM) analysis using an accelerating voltage of 80 kV. The results presented in Fig. 2a show a planar honeycomb-like atomic structure for monolayer $RuO_2$. XEDS measurements revealed that the

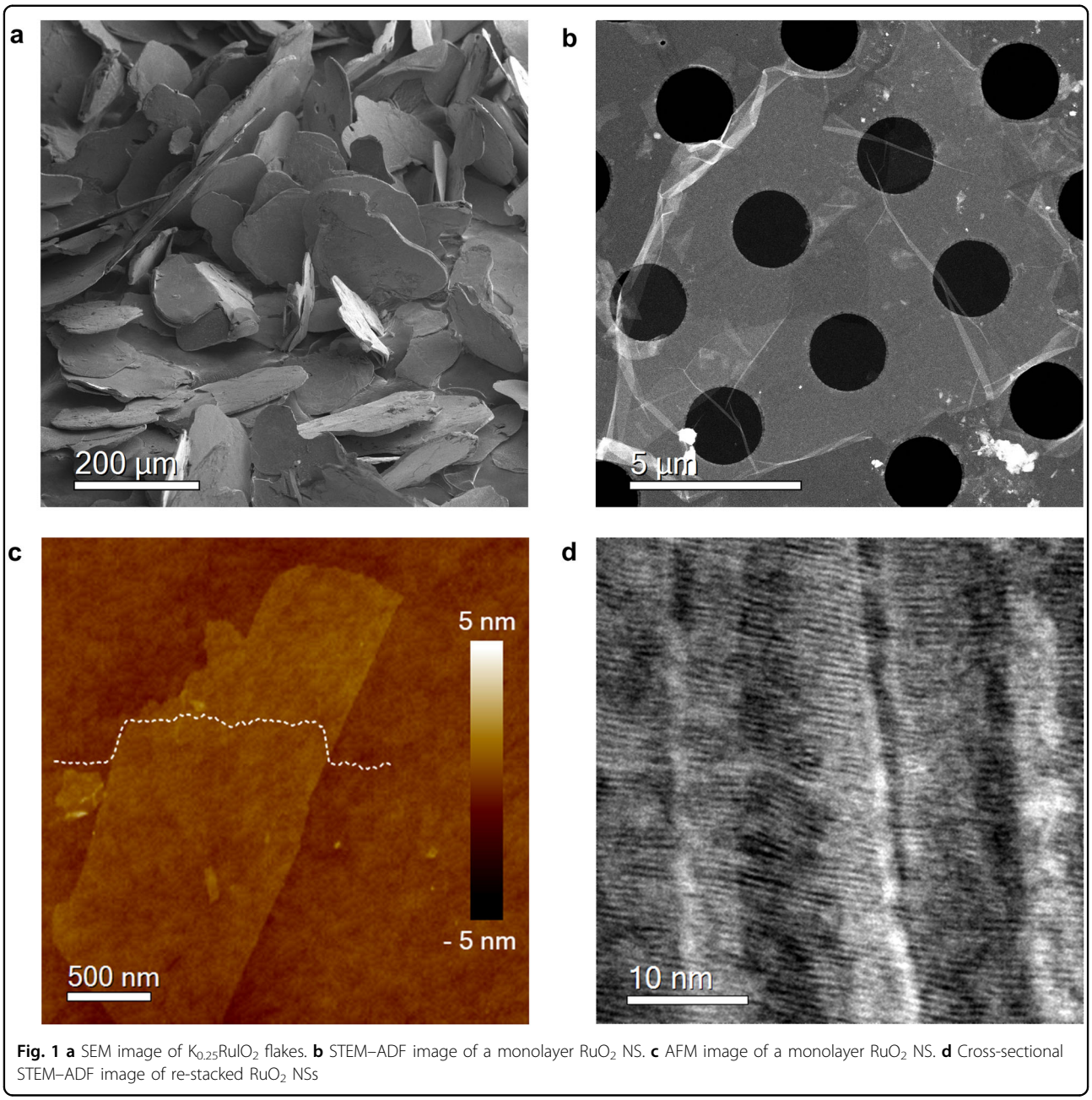


**Fig. 1** **a** SEM image of $K_{0.25}RuIO_2$ flakes. **b** STEM–ADF image of a monolayer $RuO_2$ NS. **c** AFM image of a monolayer $RuO_2$ NS. **d** Cross-sectional STEM–ADF image of re-stacked $RuO_2$ NSs

ratio of the number of Ru atoms to the number of O atoms in monolayer $RuO_2$ was close to 1:2. Furthermore, a Cs-corrected STEM–ADF image (Figure S4) revealed strong and weak signal pairs. Each strong and weak spot is attributed to one Ru atom and two O atoms, respectively. This pattern is similar to that exhibited by the Mo and S atom pairs in the *h*-$MoS_2$ crystal structure[22]. In previous reports, the crystal structure of $RuO_2$ NSs was assumed to be the same as the hexagonal structure of the parent material, K-form $RuO_2$[20,23]. However, the crystal structure observed in this study does not seem to have hexagonal symmetry. The optimal $RuO_2$ NS structure obtained from the TEM measurements and first-principles calculations is depicted in Figs. 2b and S5. It is a distorted *h*-$MoS_2$-type structure with the following in-plane lattice parameters: $a = 2.830$ Å, $b = 4.894$ Å, and $\theta = 89.14$ Å, shown in Figure S5 and Table S1. Note that the observed optimal crystal structure of monolayer $RuO_2$ is hereafter referred to as distorted *h*-$RuO_2$. For the first time, monolayer $RuO_2$ was not found to have hexagonal symmetry, and its structure is similar to that of *h*-type $MoS_2$. The distorted *h*-$RuO_2$ configuration consists of O–Ru–O′ layers, and each Ru atom is located at the center of a trigonal prism formed by six O atoms. Unlike

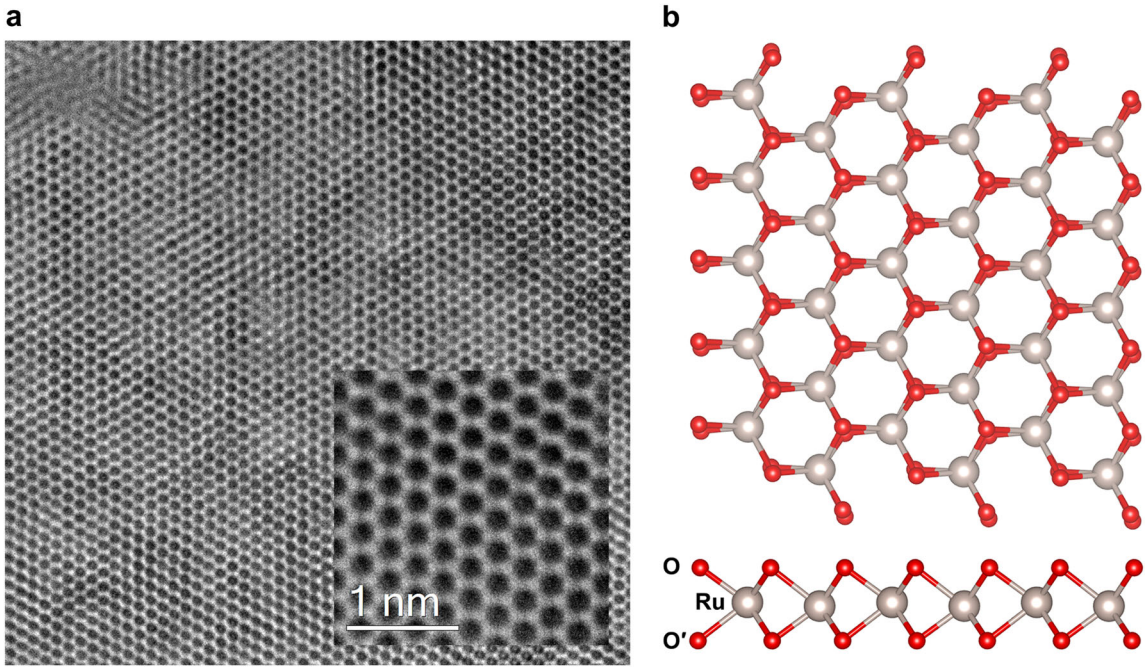


**Fig. 2 a** Monochromated Cs-corrected HRTEM image of a monolayer $RuO_2$ NS obtained using an 80 kV accelerating voltage. **b** Schematic atomic structure of monolayer a $RuO_2$ NS

*h*-$MoS_2$, the Ru layer is not flat; instead, it has a zigzag pattern along the *c*-axis (the angle between the center of the nearest Ru atoms is $\phi = 5.0°$). In addition, the top O layer is not positioned directly above the bottom O′ layer in the distorted *h*-$RuO_2$ arrangement along the *c*-axis but is slightly off center with respect to the O′ layer in the *a*–*b* plane.

As the structures of most exfoliated 2D materials, such as graphene and molybdenum disulfide, resemble those of their parents, our result that monolayer $RuO_2$ has a distorted *h*-$RuO_2$ structure is unique. As mentioned above, the parent material of $RuO_2$ NSs has *t*-type $RuO_2$ layers. This unique result can be understood by considering the structural phase transition from *t*-$RuO_2$ to distorted *h*-$RuO_2$ that occurs during chemical exfoliation. The phase transition from the *h*- to *t*-phase of transition metal dichalcogenides, such as $MoS_2$, $MoSe_2$, $WS_2$, and $WSe_2$, resulting from chemical exfoliation, was reported by Ambrosi and Duerloo[22,24]. In $RuO_2$ NSs, a reverse phase transition from *t*- to *h*-phase is expected to occur. To confirm this, we performed first-principles calculations. The calculated equilibrium lattice constants of monolayer $RuO_2$ ($a = 3.04$ Å and $b = 5.27$ Å) were ~7% larger than the experimentally observed lattice parameters ($a = 2.83$ Å and $b = 4.89$ Å), indicating that the exfoliated monolayer $RuO_2$ is under compressive strain. Structural optimizations were performed using the fixed lattice parameters listed in Table S2. Figure 3 reveals that distorted *t*-$RuO_2$ is more stable than distorted *h*-$RuO_2$ by 2.01 eV. This result raises the question of why distorted *h*-$RuO_2$ is observed rather than *t*-$RuO_2$. To answer this question, the kinetic properties of the distorted *t*- and *h*-$RuO_2$ were studied by performing nudged elastic band (NEB) calculations, which were implemented using the Vienna Ab Initio Simulation Package (VASP). As shown in Fig. 3, our NEB calculations estimated an activation energy barrier of 0.58 eV for the phase transition from distorted *h*-$RuO_2$ to distorted *t*-$RuO_2$. A recent theoretical study of $MoS_2$ showed that *h*-$MoS_2$ is more stable than *t*-$MoS_2$ by 0.8 eV, and the activation barrier of the phase transition from *t*-$MoS_2$ to *h*-$MoS_2$ is 0.79 eV[25]. Although *h*-$MoS_2$ is more stable than *t*-$MoS_2$, metastable *t*-$MoS_2$ induced by chemical exfoliation has been observed at room temperature[22,26]. This observation can be interpreted to mean that the 0.7–0.8 eV activation barrier of $MoS_2$ is sufficiently high to maintain the metastable phase even at room temperature. Similarly, it can be assumed that the distorted *h*-$RuO_2$ can be sustained in the metastable phase in monolayer $RuO_2$ because of the high activation barrier of 0.58 eV. In fact, in the TEM measurements, we observed additional bright spots at the centers of the honeycombs in the NSs (Fig. 4); however, these spots disappeared after a few seconds of exposure to the electron beam. We speculate that these spots correspond to the O atoms in the *t*-$RuO_2$ phase and that the image was taken during the phase transition from

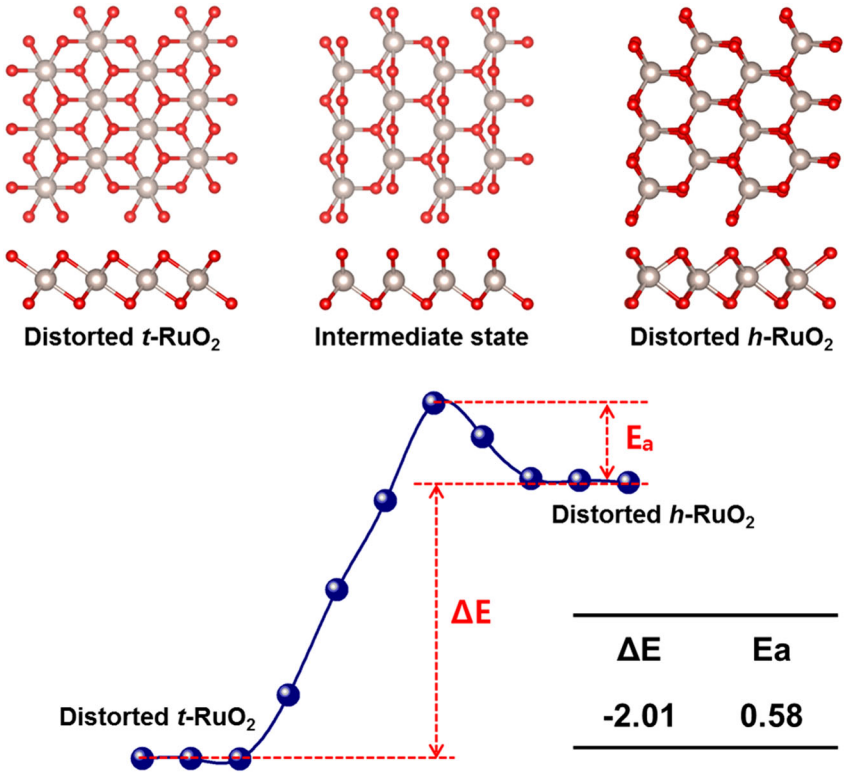


**Fig. 3** Schematic of the NEB calculation results based on the structural path of the distorted $RuO_2$ NSs during the phase transition from distorted *t*-$RuO_2$ to distorted *h*-$RuO_2$ through an intermediate state

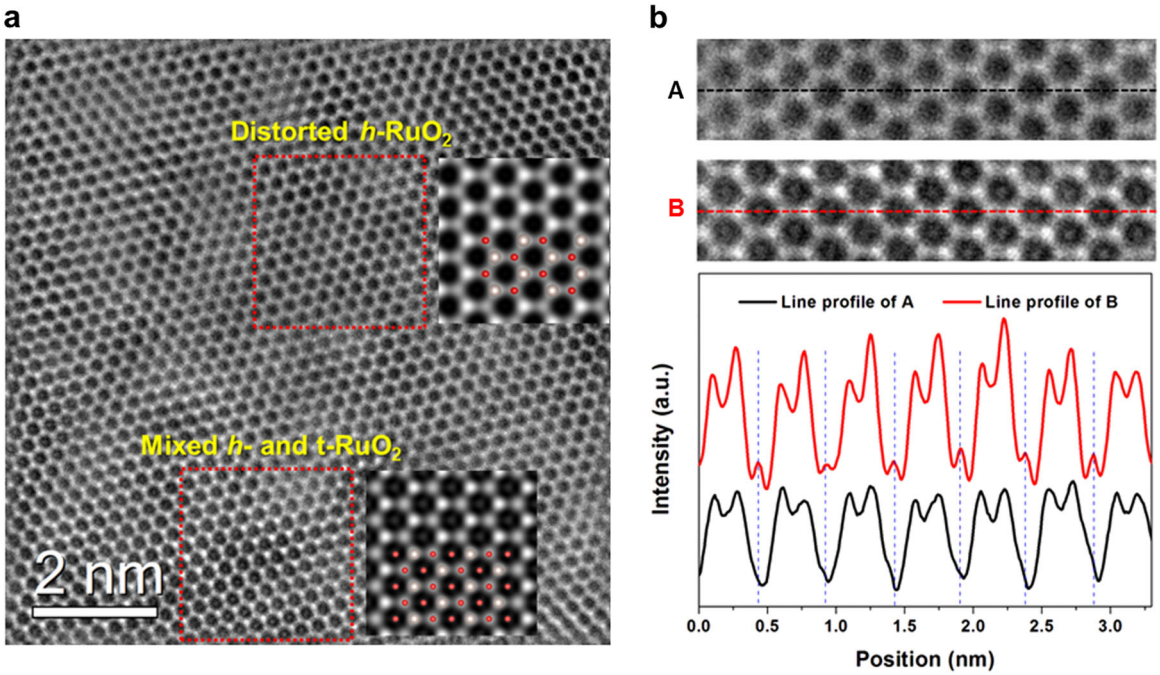


**Fig. 4 a** Monochromated Cs-corrected HRTEM image of distorted $RuO_2$ NS (insets: simulated TEM images). **b** Intensity profiles of distorted *h*-$RuO_2$ and mixed *t*- and *h*-$RuO_2$

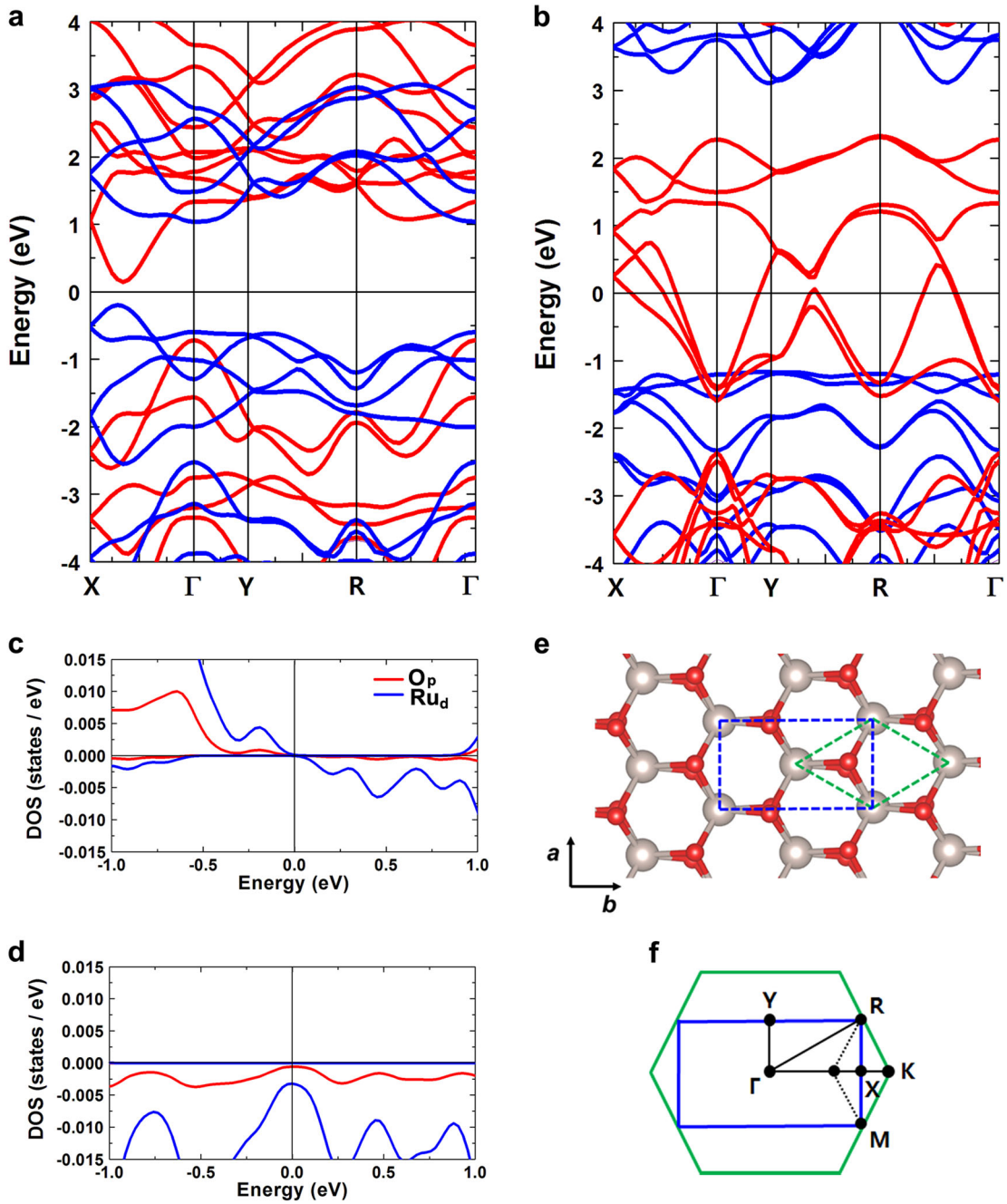


**Fig. 5** Electronic band structures and corresponding partial DOSs of **a**, **c** distorted *h*-$RuO_2$ and **b**, **d** distorted *t*-$RuO_2$. Schematic plot of **e** the crystal structure of distorted *h*-$RuO_2$ with **f** the Brillouin zone for DFT calculation. The blue and red lines in **a** and **b** indicate spin-up and spin-down states, respectively

*t*-$RuO_2$ to *h*-$RuO_2$. This hypothesis was confirmed by the simulated HRTEM images of the *t*-$RuO_2$, *h*-$RuO_2$, and mixed ($h + t$-$RuO_2$) configurations (Figs. 4 and S6), implying that an electron beam can induce the phase transition from distorted *t*-$RuO_2$ to distorted *h*-$RuO_2$, which could be additional evidence of metastable distorted *h*-$RuO_2$[27].

### Band structure calculations of distorted $RuO_2$

The electronic structures in the valence-band region of monolayer $RuO_2$ were verified by performing ultraviolet photoelectron spectroscopy (UPS) measurements on monolayer $RuO_2$ (Figure S7). The band structures of distorted *h*- and *t*-$RuO_2$ were calculated to understand the UPS data and the electrical behavior of monolayer

$RuO_2$ NSs; this is shown in Fig. 5. The calculated band structures and density of states (DOSs) suggest that distorted *t*-$RuO_2$ is a half-metal and distorted *h*-$RuO_2$ is a semiconductor with a narrow band gap of 0.35 eV. As seen in Figure S7, the experimental UPS and DOS results are in good agreement with the simulation results calculated based on the structure of distorted *h*-$RuO_2$.

The spin-polarized DFT calculations indicated that distorted *h*-$RuO_2$ NSs prefer the FM state over AFM states or non-magnetic states. Notably, the origin of magnetism in distorted *h*-$RuO_2$ NSs should be different from that of similar low-dimensional materials, such as graphene nanoribbons or hydrogenated SiC, in which the magnetism originates from chemical doping[28]. In distorted *h*-$RuO_2$ NSs, direct Ru–Ru metal–metal bonding can induce the stable FM state[29], and we plan to investigate this in our future work. We also paid special attention to the in-plane angle $\theta$ of distorted *h*-$RuO_2$ (shown in Figure S5) because we found that the calculated electrical properties were very sensitive to $\theta$. Distorted *h*-$RuO_2$ exhibits a band gap at the Dirac point owing to the lower symmetry of this structure, which has neither hexagonal nor any other crystallographic symmetry. However, if the crystallographic symmetry is higher in distorted *h*-$RuO_2$, i.e., if $\theta = 90°$ instead of 89.1°, the band gap at the Dirac point is expected to close. Thus, the electrical properties of distorted *h*-$RuO_2$ can be manipulated by changing the lattice distortion by adjusting $\theta$ (Figure S8). Similar band-gap engineering of $MoS_2$ by applying strain has been reported earlier[30,31].

### Electrical and optical properties of distorted *h*-$RuO_2$ NSs

Knowledge about the optical and electrical properties of $RuO_2$ NSs is essential for understanding their use in electronic and optoelectronic devices. Figure 6a presents the temperature dependence of the resistivity of an individual monolayer $RuO_2$ NS measured by the four-point electrode method (inset of Fig. 6a), which was used to avoid contact resistance between the $RuO_2$ NS and the electrodes. As shown in Fig. 6a, the resistivity increases with decreasing temperature, which can be understood based on the semiconducting properties. The experimental results of the electrical transport measurements support the TEM observations, and electronic band structure simulation results for distorted *h*-$RuO_2$ NSs are shown in Figs. 2a and 5a, respectively. The semiconducting electrical transport of $RuO_2$ NSs provides clear evidence of the structural phase transition from *t*- to *h*-$RuO_2$ that occurs during chemical exfoliation because rutile $RuO_2$ exhibits metallic behavior[32]. Furthermore, we observe that the resistivity increases as the number of $RuO_2$ NS layers decreases, as shown in Figure S9b. This thickness-dependent electrical transport phenomenon

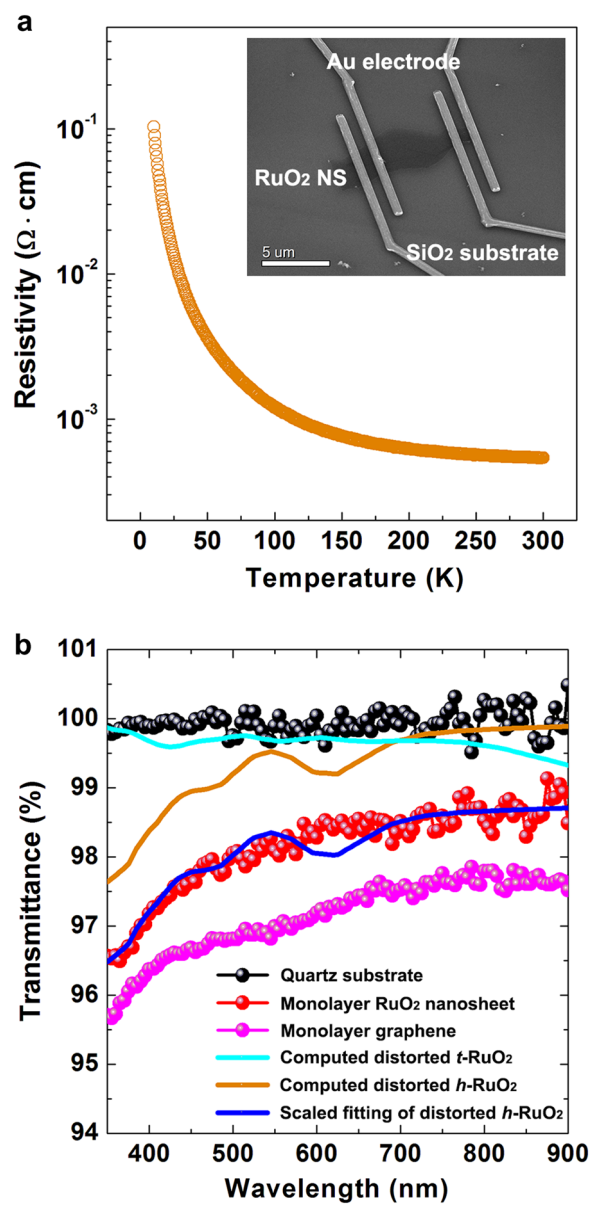


**Fig. 6 a** Resistivity vs. temperature curve of monolayer $RuO_2$ NSs (inset: SEM image of an individual $RuO_2$ NS with four electrodes). **b** Experimental transmission spectra of monolayer $RuO_2$ NS, CVD graphene, and a quartz substrate. The transmission spectra computed for distorted *h*-$RuO_2$ and *t*-$RuO_2$ and a transmission curve of distorted *h*-$RuO_2$ scaled by a factor of 0.9882 are presented

can be understood by band-gap engineering caused by quantum confinement[33] and the interfacial scattering of charge carriers[34,35]. $RuO_2$ NSs with fewer layers have higher surface-to-volume ratios; thus, thicker NSs have smaller surface defects and, consequently, lower resistivity values. The electrical properties that depend on the number of layers were discussed in more detail in one of our recent reports. Moreover, the $RuO_2$ NS films were very stable in the external electrical, mechanical, or

optical field, showing a change in the resistance of less than 1% over 50,000 bending test cycles[36].

Figures 6b and S10 illustrate the optical transmission spectra of monolayer $RuO_2$ NSs and the locations used to obtain the spectra, respectively. The transmittance $T$ of monolayer $RuO_2$ NSs is 98.3 ± 0.1% in the visible wavelength ($\lambda$) range of 450–700 nm and is practically independent of $\lambda$ above 450 nm. The average $T$ of $RuO_2$ in the visible range is ~1% higher than that of single-layer graphene grown by chemical vapor deposition (CVD). The CVD-grown graphene exhibits $T = 97.3 \pm 0.1\%$ (450 nm < $\lambda$ < 700 nm), which is comparable to that previously reported for natural graphene, $T = 97.7\%$[37]. The optical microscopy analysis further revealed that opacity increases with the number of NS, and each $RuO_2$ layer adds an additional 1.5% (see Figure S11). Figure 6b also presents the computed transmission spectra of both distorted *h*- and *t*-$RuO_2$. In addition, we simulated the transmission spectra by performing optical dielectric calculations with the HSE06 function in the VASP package assuming a thickness of 0.65 nm for each individual monolayer. We estimated the relative populations of the two $RuO_2$ structures in a single layer by fitting the experimental $RuO_2$ transmission curve with $s \times [p_1 \times T_h + p_2 \times T_t]$, where $s$ is a scaling factor, $p_i$ is the relative population with $p_1 + p_2 = 1$, and $T_h$ and $T_t$ are the computed transmission spectra of distorted *h*- and *t*-$RuO_2$, respectively. The fitted result that has best-fit parameters of $s = 0.9882$ and $p_1 = 1.00$ is represented by the blue line in Fig. 6b. The scaled transmission spectrum of distorted *h*-$RuO_2$ shows excellent agreement with the experimental one. This rough estimate suggests that distorted *t*-$RuO_2$ has a negligible contribution to the experimental transmission curve and that the monolayer $RuO_2$ NSs investigated here are mainly composed of the distorted *h*-$RuO_2$ structure. As shown by the band structure in Fig. 5a, the high $T$ of distorted *h*-$RuO_2$ may be attributed to its large optical gap within each spin state.

The electrical resistivity and optical $T$ of individual monolayer $RuO_2$ NSs were measured to be ~$5.4 \times 10^{-2}$ Ω cm and ~98.3% at room temperature, respectively, revealing that the $RuO_2$ NSs are competitive with graphene as a promising material for flexible transparent electrodes. This feasibility was demonstrated by fabricating $RuO_2$ NS films on polycarbonate films using the Langmuir–Blodgett (LB) method. The LB-deposited $RuO_2$ NS films with two layers and four layers have sheet resistances of $8.3 \times 10^3\ \Omega\ sq^{-1}$ and $3.2 \times 10^3\ \Omega\ sq^{-1}$ with optical $T$ values of 97.2% and 93.4%, respectively. Moreover, the foldability and electrical connectivity were investigated by using a blue light-emitting diode (LED) bulb connected to the four-layer LB-deposited $RuO_2$ NSs films. The light of the LED remained on when the $RuO_2$ NS films were folded, as shown in Figure S12. Considering that chemically exfoliated graphene LB films have sheet resistances of ~$8 \times 10^3\ \Omega\ sq^{-1}$ with an optical $T$ of 98%, our results demonstrate that the $RuO_2$ NS films are competitive as flexible transparent electrodes owing to their low sheet resistance, high optical transparency, and mechanical flexibility. The temperature-dependent electrical properties of the $RuO_2$ NSs films were investigated using a physical property measurement system (PPMS). The activation energy of $RuO_2$ NS films was calculated from the Arrhenius equation ($\sigma = A\ \exp(-E_a/K_b T)$, where $A$ is the pre-exponential factor; $E_a$ is the experimental activation energy; $K_b$ is the Boltzmann constant). The calculated activation energy was ~0.14 eV as shown in Figure S13, meaning that the $RuO_2$ NS films have narrow band-gap semiconductor behavior. This result considerably agrees with the simulation results of the simulation based on the structure of distorted *h*-$RuO_2$.

## Conclusion

In summary, we identified the crystal structure of monolayer $RuO_2$ NSs as distorted *h*-$RuO_2$ by experimental observations and computational calculations. We showed that the structural phase transition from the *t*- to *h*-phase occurs under compressive strain during the chemical exfoliation process, and this structural phase transition causes a difference in the electrical and optical properties between the nanosheet and its parent material. The $RuO_2$ NS exhibits narrow band-gap semiconducting behavior, while the parent material of $K_{0.25}RuO_2$ exhibits metallic properties. Furthermore, the electrical resistivity and optical $T$ of individual monolayer $RuO_2$ NSs are ~$5.4 \times 10^{-2}$ Ω cm and ~98.3% at room temperature, respectively, indicating that distorted *h*-$MX_2$ $RuO_2$ NSs can compete with graphene. Moreover, we presented that the LB-deposited $RuO_2$ NS films act as flexible transparent electrodes with high foldability. Our results showed that the electrical properties of monolayer $RuO_2$ can be manipulated by adjusting the structural distortions, suggesting the possibility of band-gap engineering in nanostructured materials.

## Methods

### Materials synthesis

Potassium ruthenate (K-form $RuO_2$) layered structures were synthesized by annealing a mixture of $K_2CO_3$ and $RuO_2$ at 850 °C under a flow of $N_2$ for 24 h using a furnace. The chemical composition ratio of K-form $RuO_2$ was experimentally confirmed by inductively coupled plasma-atomic emission spectroscopy (ICP-AES), energy-dispersive spectroscopy (EDS), and X-ray photoelectron spectroscopy (XPS) investigations showing the measured ratio of K:Ru:O is 0.23–0.27:1:1.92–2.05. The K-form $RuO_2$-layered structures were acquired by washing the annealed samples with deionized water. The K-form

$RuO_2$ particles were immersed in 1 M HCl for 72 h to replace their $K^+$ ions with $H^+$ ions. The interlayer $K^+$ ions were exchanged by immersing the particles in 1 M HCl for 3 days at 60 °C. The acid-treated K-form-layered protonic $RuO_2$ structures were exfoliated by the intercalation of tetrabutylammonium hydroxide. The solutions were gently stirred for 14 days at room temperature to exfoliate the $H_{0.2}RuO_2$ to $RuO_2$ NSs (Fig. 1c). The monolayer NSs were collected, and the non-exfoliated particles were removed by centrifuging at 2000 rpm for 30 min.

### Microstructural analysis

The HRTEM and STEM–ADF images of the $RuO_2$ NSs were acquired by using a double-Cs-corrected Titan Cubed microscope equipped with a monochromator operated at an accelerating voltage of 80 kV. The resolution of the Cs-corrected HRTEM images (<90 pm) was sufficient to observe the atomic structure of the $RuO_2$ NSs (the shortest atomic length of Ru–O is ~160 pm). Furthermore, the monochromator performance at low accelerating voltages, such as 80 kV, is pivotal in HRTEM imaging. It not only improves the image resolution by correcting chromatic aberration, but also avoids knock-on electron-beam damage and enhances the contrast of O because the scattering power is higher at lower voltages. The HRTEM images were obtained by activating the monochromator to achieve an energy spread of 0.1 eV. The convergence and detector semi-angles of 30 mrad and 65–200 mrad, respectively, were used to acquire the STEM–ADF images. The TEM analysis of $K_{0.25}RuO_2$ and $NaRuO_2$ was performed by using a Cs-corrected Titan G2 80–200 microscope with a Super-X$^{TM}$ XEDS detector at 200 kV. The atomic position of O was observed by using the STEM–ABF technique with convergence and detector semi-angles of 26 mrad and 12–24 mrad, respectively. The simulated HRTEM images were obtained using the HREM simulation suite (HREM Research Inc., $C_S = 1$ μm under Scherzer defocus). The AFM measurements were performed in tapping mode using rectangular Si cantilevers (spring constant, $k = 40\ \mathrm{N\,m^{-1}}$, and resonance frequency,
$f = 300$ kHz) under ambient conditions with a Dimension Icon microscope (Brucker). The conventional XRD measurements of the bulk $K_{0.25}RuO_2$ powder were conducted by applying Cu Kα radiation with $\lambda = 1.54$ Å. The unknown $K_{0.25}RuO_2$ crystal structure was determined using the Rietveld refinement technique, and the structural optimization was performed based on first-principles calculations.

### Optical characteristics

The optical transmission spectra and NS images were obtained using a UV-vis absorption spectrometer capable of microscopic characterization (QDI 2010, Craic Technologies Inc., USA). White light from a Xe lamp was used to illuminate the samples, and the optical images of the 2D NSs on a quartz substrate (1″ × 1″, 1 mm thick) were collected using an imaging lens (×40, 0.6 NA) and a charge-coupled device camera. For the transmission measurements, a small part of the transmitted light was directed to a spectrometer before it reached the camera (dark square in Figure S10 with dimensions of 6 μm × 6 μm). The transmission spectra presented in this report were averaged over 250 scans. Independently measured background spectra from NS-free regions of the quartz substrate were subtracted from the sample spectra, as in Figure S10. The dispersed $RuO_2$ NSs and CVD-grown graphene flakes were prepared on the quartz substrate by drop-casting and the standard transfer methods, respectively. All measurements were performed under ambient conditions.

### Device fabrication and electronic characteristics

Single $RuO_2$ NSs were fabricated using electron-beam lithography (JSM-7001F JEOL and ELPHY Quantum Raith). The synthesized $RuO_2$ NSs were dispersed by drop-casting on a thermally oxidized Si (100) substrate with alignment markers patterned for electron-beam lithography. The position and orientation of a selected NS was defined by the digitized coordinates obtained from a scanning electron microscopy (SEM) image. Cr (5 nm)/Au (50 nm) electrodes were deposited using a custom-made, ultra-high-vacuum DC sputtering system. The resistance of each individual $RuO_2$ NS was determined by performing four-probe measurements to prevent contact resistance between the NSs and the electrodes. The resistivity of each $RuO_2$ NS was calculated by using the equation $\rho = R\pi(d/2)2/L$, where $R$ and $L$ are the resistance and channel length, respectively. The temperature-dependent resistivity was obtained in the temperature range of 10–300 K using a closed-cycle cryostat. All measurements were conducted in a high vacuum with a pressure of less than $5 \times 10^{-6}$ Torr to eliminate convectional thermal fluctuations. The UPS measurements were performed using a custom-made in situ analysis system (UV generator: VUV 5000 and electron detector: SES-100). The electrical conductivity of the $RuO_2$ NS films was measured using a physical property measurement system (PPMS DynaCool, Quantum Design).

### First-principles calculations

We performed the first-principles calculations to investigate the structural stability and electronic structure of $RuO_2$, using VASP and a projector-augmented wave (PAW) pseudo-potential. In the PAW pseudo-potential, the 2*s* and 2*p* electrons and the 4*s* and 4*d* electrons were treated as the valence states of O and Ru, respectively.

The exchange-correlation effects were described by the generalized gradient approximation functional of Perdew, Burke, and Ernzerhof, and the spin-polarization effects were considered. An exact description of the Ru *d*-electron states was obtained by performing hybrid density-functional theory calculations (screened hybrid functional by Heyd, Scuseria, and Ernzerhof (HSE06)) with a mixing ratio of 0.25 for an exact exchange interaction. For the total energy calculations, a plane-wave basis set with a kinetic energy cutoff of 400 eV and an $8 \times 4 \times 1$ Monkhorst–Pack k-point grid including a gamma point were used. The structure was optimized by performing structural relaxation until the total energy difference was less than $10^{-5}$ eV. The structural phase transition of $RuO_2$ was investigated by using the NEB method, as implemented in VASP. The conductivity of $RuO_2$ was calculated by employing the BoltzTrap program, which is compatible with VASP, with a constant-scattering-time approximation. In this case, denser k-point grids generated by a $32 \times 16 \times 2$ Monkhorst–Pack mesh were used to calculate the electronic structure in detail. A scattering time $\tau$ of $1 \times 10^{-14}$ s was used. We estimated the optical properties by calculating the frequency-dependent dielectric function using HSE06 functions and VASP. The dielectric function can be expressed as the sum of real and imaginary parts: $\varepsilon(\omega) = \varepsilon'(\omega) + i\varepsilon''(\omega)$. The use of this function and the relation $\sqrt{\varepsilon} = n + iK$, where $n$ is the refractive index and $K$ is the extinction coefficient, enables us to obtain $K(\varepsilon'(\omega), \varepsilon''(\omega))$. From $K(\varepsilon'(\omega), \varepsilon''(\omega))$, the absorption coefficient $\alpha$ ($\alpha = 4\pi K(\omega)/\lambda$) and the transmittance $T$, which can be expressed as $T = \exp(-\alpha t)$, where $t$ is the thickness of a $RuO_2$ monolayer (0.65 nm), were obtained from the experimental results.

**Acknowledgements**
We thank Prof. B. J. Yang, Prof. K. Lee, and Dr. E. Cho for advising the manuscript.

**Author details**
[1]Platform Technology Lab, Samsung Advanced Institute of Technology, 130 Samsung-ro, Yeongtong-gu, Suwon-si, Gyeonggi-do 16678, Republic of Korea. [2]Inorganic Materials Lab, Samsung Advanced Institute of Technology, 130 Samsung-ro, Yeongtong-gu, Suwon-si, Gyeonggi-do 16678, Republic of Korea. [3]Department of Materials Science and Engineering, Yonsei University, 50 Yonsei-ro, Seodaemun-gu, Seoul 03722, Republic of Korea. [4]School of Nano & Materials Science and Engineering, Kyungpook National University, 2559 Gyeongsang-daero, Gyeongsangbuk-do 37224, Republic of Korea

**Conflict of interest**
The authors declare that they have no conflict of interest.

**Publisher's note**
Springer Nature remains neutral with regard to jurisdictional claims in published maps and institutional affiliations.

**Supplementary information** is available for this paper at https://doi.org/10.1038/s41427-018-0020-y.

Received: 2 August 2017 Revised: 22 November 2017 Accepted: 10 December 2017
Published online: 16 April 2018

**References**

1. Novoselov, K. S. et al. Electric field effect in atomically thin carbon films. *Science* **306**, 666–669 (2004).
2. Novoselov, K. S. et al. Two-dimensional atomic crystals. *PNAS* **30**, 10451–10453 (2005).
3. Xu, M., Liang, T., Shi, M. & Chen, H. Graphene-like two-dimensional materials. *Chem. Rev.* **113**, 3766–3798 (2013).
4. Miró, P., Audiffred, M. & Heine, T. An atlas of two-dimensional materials. *Chem. Soc. Rev.* **43**, 6537–6554 (2014).
5. Fiori, G. et al. Electronics based on two-dimensional materials. *Nat. Nanotechnol.* **9**, 768–779 (2014).
6. Gao, S. et al. Partially oxidized atomic cobalt layers for carbon dioxide electroreduction to liquid fuel. *Nature* **529**, 68–71 (2016).
7. Akhavan, O. & Ghaderi, E. Photocatalytic reduction of graphene oxide nanaosheets on $TiO_2$ thin film for photoinactivation of bacteria in solar light irradiation. *J. Phys. Chem. C* **113**, 20214–20220 (2009).
8. Hu, C.-C., Chang, K.-H., Lin, M.-C. & Wu, Y.-T. Design and tailoring of the nanotubular arrayed architecture of hydrous $RuO_2$ for next generation supercapacitors. *Nano Lett.* **6**, 2690–2695 (2006).
9. Wu, Z. et al. Graphene/metal oxide composite electrode materials for energy storage. *Nano Energy* **1**, 107–131 (2012).
10. Xu, J., Wang, K., Zu, S., Han, B. & Wei, Z. Hierarchical nanocomposites of polyaniline nanowire arrays on graphene oxide sheets with synergistic effect for energy storage. *ACS Nano* **4**, 5019–5026 (2010).
11. Xu, J.-J. et al. Cathode surface-induced, solvation-mediated, micrometer-sized $Li_2O_2$ cycling for Li-$O_2$ batteries. *Adv. Mater.* **28**, 9620–9628 (2016).
12. Chang, Z.-W., Xu, J.-J., Liu, Q.-C., Li, L. & Zhang, X.-B. Recent progress on stability enhancement for cathode in rechargeable non-aqueous lithium-oxygen battery. *Adv. Energy Mater.* **5**, 1500633 (2015).
13. Liu, T. et al. Ultrathin, lightweight, and wearable Li-$O_2$ battery with high robustness and gravimetric/volumetric energy density. *Small* **13**, 1602952 (2017).
14. Yang, X.-Y. et al. High-performance integrated self-package flexible Li-$O_2$ battery based on stable composite anode and flexible gas diffusion layer. *Adv. Mater.* **29**, 1700378 (2017).
15. Shikano, M., Delmas, C. & Darriet, J. $NaRuO_2$ and $Na_xRuO_2.yH_2O$: new oxide and oxyhydrate with two dimensional $RuO_2$ layers. *Inorg. Chem.* **43**, 1214–1216 (2004).
16. Fukuda, K., Kato, H., Sato, H., Sugimoto, W. & Takasu, Y. Swelling, intercalation, and exfoliation behavior of layered ruthenate derived from layered potassium ruthenate. *J. Solid State Chem.* **182**, 2997–3002 (2009).
17. Wang, C. et al. All-nanosheet ultrathin capacitors assembled layer-by-layer via solution-based processes. *ACS Nano* **8**, 2658–2666 (2014).
18. Lee, S. et al. Superior additive of exfoliated $RuO_2$ nanosheet for optimizing the electrode performance of metal oxide over graphene. *J. Phys. Chem. C* **120**, 11786–11796 (2016).
19. Choi, S.-J., Jang, J.-S., Park, H. P. & Kim, I.-D. $NO_2$ sensors: optically sintered 2D $RuO_2$ nanosheets: temperature-controlled $NO_2$ reaction. *Adv. Funct. Mater.* **27**, 1606026 (2017).
20. Boman, C. Refinement of the crystal structure of ruthenium dioxide. *Acta Chem. Scand.* **24**, 116 (1970).
21. Zhi, C., Bando, Y., Tang, C., Kuwahara, H. & Golberg, D. Large-scale fabrication of boron nitride nanosheets and their utilization in polymeric composites with improved thermal and mechanical properties. *Adv. Mat.* **21**, 2889 (2009).
22. Ambrosi, A., Sofer, Z. & Pumera, M. 2H → 1T phase transition and hydrogen evolution activity of $MoS_2$, $MoSe_2$, $WS_2$ and $WSe_2$ strongly depends on the $MX_2$ composition. *Chem. Commun.* **51**, 8450–8453 (2015).
23. Shi, L., Xu, A. & Zhao, T. $RuO_2$ monolayer: a promising bifunctional catalytic material for nonaqueous lithium-oxygen batteries. *J. Phys. Chem. C* **120**, 6356–6362 (2016).
24. Duerloo, K.-A. N., Li, Y. & Reed, E. J. Structural phase transitions in two-dimensional Mo- and W-dichalcogenide monolayers. *Nat. Commun.* **5**, 4214 (2014).
25. Esfahani, D. N., Leenaerts, O., Sahin, H., Partoens, B. & Peeters, F. M. Structural transitions in monolayer $MoS_2$ by lithium adsorption. *J. Phys. Chem. C* **119**, 10602–10609 (2015).

26. Eda, G. et al. Coherent atomic and electronic hetero structures of single-layer $MoS_2$. *ACS Nano* **6**, 7311–7317 (2012).
27. Lin, Y.-C., Dumcenco, D. O., Huang, Y.-S. & Suenaga, K. Atomic mechanism of the semiconducting-to-metallic phase transition in single-layered $MoS_2$. *Nat. Nanotechnol.* **9**, 391–396 (2014).
28. Li, X., Wu, X., Li, Z., Yang, J. & Hou, J. G. Bipolar magnetic semiconductors: a new class of spintronics materials. *Nanoscale* **4**, 5680–5685 (2012).
29. Whangbo, M.-H. & Canadell, E. Analogies between the concepts of molecular chemistry and solid-state physics concerning structural instabilities. Electronic origin of the structural modulations in layered transition metal dichalcogenides. *J. Am. Chem. Soc.* **114**, 9587 (1992).
30. Castellanos-Gomez, A. et al. Local strain engineering in atomically thin $MoS_2$. *Nano Lett.* **13**, 5361–5366 (2013).
31. Conley, H. J. et al. Bandgap engineering of strained monolayer and bilayer $MoS_2$. *Nano Lett.* **13**, 3626–3630 (2013).
32. Ryden, W. D. & Lawson, A. W. Temperature dependence of the resistivity of $RuO_2$ and $IrO_2$. *Phys. Lett. A* **26**, 209–210 (1968).
33. Kuc, A., Zibouche, N. & Heine, T. Influence of quantum confinement on the electronic structure of the transition metal sulfide $TS_2$. *Phys. Rev. B* **83**, 245213 (2011).
34. Radisavljevic, B. & Kis, K. Mobility engineering and a metal-insulator in monolayer $MoS_2$. *Nat. Mater.* **12**, 815–820 (2013).
35. Li, S. et al. Thickness-dependent interfacial Coulomb scattering in atomically thin field-effect transistors. *Nano. Lett.* **13**, 3546–3552 (2013).
36. Yoo, S. et al. Strong enhancement of electrical conductivity in two-dimensional micrometer-sized $RuO_2$ nanosheets for flexible transparent diodes. *Nanoscale* **9**, 7104–7113 (2017).
37. Nair, R. R. et al. Fine structure constant defines visual transparency of graphene. *Science* **320**, 1308 (2008).